PERGAMON

Chemical Engineering Science 55 (2000) 3287–3303

Chemical Engineering Science

Turbulent flow in stirred vessels agitated by a single, low-clearance hyperboloid impeller

F. T. Pinho[a,*], F. M. Piqueiro[b], M. F. Proença[b], A. M. Santos[c]

[a]*Centro de Estudos de Fenómenos de Transporte, DEMEGI, Faculdade de Engenharia, Rua dos Bragas, 4050-123 Porto, Portugal*
[b]*Departamento de Engenharia Civil, Faculdade de Engenharia, Rua dos Bragas, 4050-123 Porto, Portugal*
[c]*Instituto de Engenharia Mecânica e Gestão Industrial, Unidade de Térmica Industrial, Rua do Barroco 174, 4465-591 S. Mamede de Infesta, Portugal*

Received 11 January 1999; accepted 10 September 1999

Abstract

Detailed angle-resolved measurements of the mean and rms of the three components of the velocity vector were carried out by laser-Doppler anemometry in a stirred vessel mechanically agitated by a ribbed, low power consumption hyperboloid impeller at a Reynolds number of 50,000. Due to the small clearance of the agitator the flow pattern in the vessel was typical of that encountered when using an axial turbine although the flow in the vicinity of the impeller was alike that in a radial device with the mean flow discharge following a λ- type pattern. In most of the vessel the flow was gentle with mean velocities of the order of 5% of the tip velocity, increasing to about 20% V_{imp} towards the tip of the impeller because of the ribs. Their small size limited the extent of periodic flow to a region delimited by the bottom and $z/R = 0.2$ in the vertical direction, and $r/R = 0.85$–1.4 in the radial direction, plus the volume below the impeller. In these regions the turbulence was not isotropic and reached the highest values so that the maximum turbulence kinetic energy was 65% higher than for the corresponding hyperboloid flow in the absence of shear ribs.

Keywords: Mixing vessel; Hyperboloid impeller; Periodic flow

1. Introduction

Stirred vessel flows can rely on conventional agitators, such as the Rushton or pitched blade turbine, or on especially designed impeller geometries as is the case of the hyperboloid. This impeller was developed by Höfken, Bischof and Durst (1991) from considerations of fluid dynamics aimed at ensuring a complete suspension of particles and a good dispersion of air bubbles, and it was designed for application in waste water treatment plants (Höfken, Zahringer & Bischof, 1994). Sludge treatment requires gentle agitation without destruction of suspended micro-organisms, which otherwise could stop the chemical process. Designs other than conventional ones can be better at specific tasks, as Buckland, Gbewonyo, DiMasi, Hunt, Westerfield and Nienow (1988) and Bakker and Van den Akker (1990) have shown relative to gas dispersion with hydrofoils.

The investigation of the performance of an agitator should proceed in various steps: initially there should be an assessment of the overall flow features, such as flow patterns and power consumption, which for this impeller was first carried out by Nouri and Whitelaw (1994) and Ismailov, Schäfer, Durst and Kuroda (1997). Both investigated the flow generated by the hyperboloid impeller with eight transport ribs on its upper surface and different clearances from the bottom of the vessel. It is usually necessary to provide aeration for the processes and the presence of shear ribs at the lower surface of the impeller can improve bubble break-up but the extent of this effect needs to be investigated. Both transport and shear ribs and a small clearance were geometrical features of the hyperboloid impeller investigated by Pinho, Piqueiro, Proença and Santos (1997), who found that the power number varied from 0.5 for a $D/T = 0.78$ impeller to 0.95 for a $D/T = 0.24$ impeller, as compared to a value of 5 for the Rushton stirrer at identical high Reynolds number flows. A comparison with Ismailov et al. (1997) shows that the presence of the shear ribs is responsible for an increase in the power consumption of the order of 250%.

* Corresponding author. Tel.: + 351-22-200-3628; fax: + 351-22-953-7352.
E-mail address: fpinho@fe.up.pt (F. T. Pinho)

0009-2509/00/$ - see front matter
PII: S0009-2509(99)00570-9

Gas or liquid dispersion is highly dependent on the turbulent Kolmogorov microscale, therefore it is important to perform detailed mean and turbulent kinematic measurements from which the dissipation rate, and thence the minimum drop size, can be determined. This has been the motivation for recent investigations with conventional agitators (Mujumdar, Huang, Wolf, Weber & Douglas, 1970; Laufhütte & Mersmann, 1985; Costes & Couderc, 1988; Wu & Patterson, 1989; Kresta & Wood, 1993), which were initiated as early as the sixties when Cutter (1966) performed its detailed energy balance from measured data. Detailed information on the turbulent flow field is also relevant to the kinetics of aggregates, as is well shown by the works of Nouri and Whitelaw (1992) and especially Kusters (1991) and to provide guidelines on the location of feed pipes as is known that mixing times can be reduced by proper injection of the additives in regions of very high turbulence.

These objectives can be fulfilled by extensive measurements such as those of Reed, Princz and Hartlard (1977) and Yianneskis, Popiolek and Whitelaw (1987) who helped in the understanding of the physics of the flow in vessels powered by the Rushton turbine. The latter work showed well the flow separation behind the Rushton blades with their angle-resolved measurements and concluded that the turbulent kinetic energy in the radial jet emanating from the impeller was 10 times higher than that in the remaining regions of the vessel. By performing angle-resolved measurements close to the impeller these workers were also able to show that previous research, unaware of the periodicity effects created by the passage of the blades, could overestimate the turbulent quantities by as much as 400%.

Other detailed measurements have been carried out aimed at understanding the influence of geometric parameters, such as the recent investigations of Rutherford, Mahmoudi, Lee and Yianeskis (1996a,b), which assessed the impeller blade thickness effect, or the impact of tank geometry on dissipation rate by Zhou and Kresta (1996), amongst others.

The work to be presented here is the obvious complement to the previous investigations of Nouri and Whitelaw (1994), Ismailov et al. (1997), Piqueiro, Proença, Pinho and Santos (1996) and Pinho et al. (1997). In particular, in the two latter works the mean flow features have been well characterised and some turbulent flow properties were presented in the vicinity of the hyperboloid impeller for the same flow configuration and impeller geometry. An improved understanding of the behaviour of the hyperboloid impeller requires not only the detailed turbulent information to be presented below but also some information on process engineering whose investigation is currently under way.

In the next section the experimental facility, the measuring procedures and their uncertainties are described, and the report is followed by the presentation and discussion of the results. In the results section the data are processed in various ways to yield important information. This paper ends with a summary of the main findings and an outline of the next phases of the work to be performed.

2. Experimental set-up

2.1. Experimental rig

The experimental rig, schematically represented in Fig. 1, consisted of a 292 mm diameter T stirred vessel in acrylic, which was mounted on a support standing directly on top of a 3-D milling table, as already described in Pinho et al. (1997). The vessel allowed a maximum height of liquid of 600 mm, but the work reported here concerns a fluid height H of 300 mm ($H/T = 1$). The vessel was mounted inside a square trough filled with the same liquid in order to reduce optical refractions and help maintain a constant temperature in the bath. Within the tank, four 25 mm wide and 4 mm thick baffles were mounted at 90° intervals to avoid solid-body rotation of the fluid. To eliminate the dead zones behind the baffles these were attached to small triangular connectors fixed to the vessel wall to create a 6 mm gap. The bottom of the tank was flat and had a bearing embedded in it to support the drive shaft.

The 100 mm diameter D hyperboloid impeller was supplied by Invent GmbH and was mounted on the 5 mm diameter shaft. The impeller had eight transport ribs on its upper surface and 24 shear ribs located at the edge of the bottom surface. It was mounted close to the bottom, defining a clearance to vessel diameter ratio C/T of 1/30 (c.f. Fig. 1) and the height of the ribs B was equal

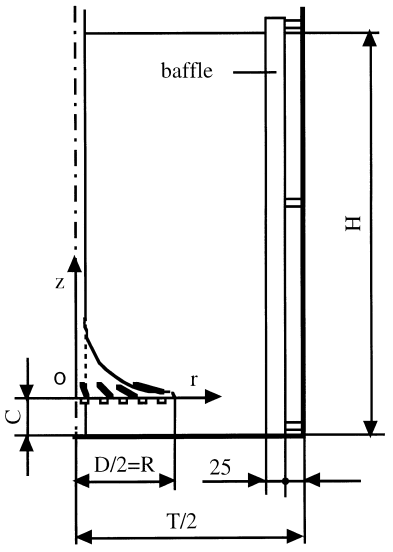

Fig. 1. The stirred vessel and the co-ordinate system.

to 5 mm ($B/R = 0.1$). More details on the impeller geometry can be found in Höfken and Bischof (1993) and Pinho et al. (1997).

To power the impeller, a 600 W DC Servo motor was used which was controlled by a variable power supply unit. A tachogenerator gave an electrical impulse proportional to the speed of the impeller and was connected to an amplifier as part of a speed control system feeding back the power supply unit. The tachogenerator had an analogue output of 0–10 V, corresponding to 0–3000 rpm and the velocity could also be monitored on a proper display. As a result, the speed could be kept constant with an uncertainty of around $\pm$ 1 rpm, which corresponded to less than 0.2% of the rotational speed.

2.2. Laser- Doppler anemometer characteristics

A one component Laser-Doppler anemometer from Dantec was used in the forward and backward scatter modes for measuring the three components of the mean velocity flow field in one of the tested configurations. The beam from the multimode operated 100 mW Ar-ion laser passed through a series of optical elements before the Bragg cell, where a frequency shift of 0.6 MHz was imposed. To improve the alignment of the optics and reduce the size of the control volume a pinhole section and beam expander, with an expansion factor of 1.95, were put before the 600 mm front lens.

The scattered light from titanium dioxide 3 μm mean diameter seeding particles, supplied by TSI Inc was collected by the photo-multiplier before which stood an interference filter of 514.5 nm. After being band-pass filtered the signal from the photo-multiplier was processed by a TSI 1990C counter operating in the single measurement per burst mode with a frequency validation setting of 1% in the 10/16 cycle comparison. A 1400 Dostek card interfaced the counter with a 80486-based computer which provided all the statistical quantities via a purpose-built software.

The refraction of the laser beams in the plane and curved walls was calculated and taken into account to correct the positioning of the control volume. Table 1 provides the main characteristics of the Laser- Doppler anemometer.

Far from the impeller the flow was found to be angle-independent, as shown by Piqueiro et al. (1996), and so 360° ensemble-averaged measurements were carried out and the mean and rms values were calculated from a sample size of 30,000 valid readings. This large sample was necessary for accurate results because of the low velocities and high levels of turbulence encountered in the region.

Close to the impeller, where the flow was found to be angle-dependent, measurements were synchronised with the position of the impeller and a total sample size of 600,000 points was taken. The large sample was necessary to yield accurate 1° angle-resolved measurements, calculated from an average sample of 1666 readings per 1° window.

Table 1
Main characteristics of the laser-Doppler anemometer in air at e^{-2} intensity

Laser wavelength	514.5 nm
Measured half angle of beams in air	3.65°
Dimensions of measuring volume in air	
Major axis	2.53 mm
Minor axis	162 μm
Fringe spacing	4.041 μm
Frequency shift	0.6 MHz

In the regions of high flow periodicity, near Rushton and pitched blade impellers, Yianneskis et al. (1987) and Schäfer, Yianneskis, Wachter and Durst (1998) have shown that consideration of ensemble average quantities over-predict turbulent quantities by as much as 400%. However, it is sometimes useful to characterise these regions by a single average value and for this purpose the weighted-average mean and variance values calculated by Eqs. (1) and (2), respectively, are preferred. This is especially relevant for the rms quantities since the weighted-average variance $\overline{u'^2_w}$ is equivalent to a weighted average of the 1° angle-resolved ensemble-average variance values $\overline{u'^2_\theta}$. The weighted-average variance is lower than the maximum local variance and is a more representative value of average turbulence than the total ensemble-average variance $\overline{u'^2_w}$ which suffers from considerable broadening effects, as confirmed with the present measurements taken in the vicinity of the impeller (see Appendix for more details).

$$\overline{U_w} = \frac{\sum_{\theta=1}^{360} U_\theta N_\theta}{\sum_{\theta=1}^{360} N_\theta}, \tag{1}$$

$$\overline{u'^2_w} = \frac{\sum_{\theta=1}^{360} \overline{u'^2_\theta} N_\theta}{\sum_{\theta=1}^{360} N_\theta}. \tag{2}$$

In Eqs. (1) and (2) U_θ, $\overline{u'^2_\theta}$ and N_θ represent the 1° angle-resolved ensemble averaged values of the mean velocity, variance of the velocity and sample size at each location θ, respectively.

The various sources of uncertainty in the measuring system were taken into account to calculate the total measuring uncertainty for the mean and rms velocities, as outlined in Durst, Melling and Whitelaw (1981) and Coleman and Steele (1989). The total Doppler variance (σ_D^2) is only affected by precision error and the broadening is given by Eq. (3), where the various relevant terms have the following meaning, assuming total independence and randomness of each contribution:

$$\sigma_D^2 = \sigma_{\text{vel}}^2 + \sigma_T^2 + \sigma_g^2 + \sigma_I^2 + \sigma_{\text{oth}}^2, \tag{3}$$

Table 2
Maximum uncertainties in mean velocities

Sources of uncertainty	Bias error ΔP	Precision error far from impeller	Precision error near impeller	Reference
Averaging process and amplitude effect	+ 2% (high turbulence)	–	–	Vafidis (1985)
Statistical	–	$1.98\times\frac{\sigma/\mu_s}{\sqrt{30000}}\times 100 = 1.2\%$ for 100% turbulence intensity	$1.98\times\frac{\sigma/\mu_s}{\sqrt{13330}}\times 100 = 1.7\%$ for 100% turbulence intensity	Yanta and Smith (1973)

Table 3
Maximum uncertainties in the rms of fluctuating velocities

Source of uncertainty	Precision error far from impeller	Precision error near impeller	Reference
Clock accuracy (σ_l)	$\frac{0.6}{16\times 250}\times 100 = 0.015\%$	$\frac{0.6}{16\times 250}\times 100 = 0.015\%$	TSI (1988)
Statistical (σ_{oth})	$1.98\times\frac{1}{\sqrt{2\times 30000}}\times 100 = 0.8\%$	$1.98\times\frac{1}{\sqrt{2\times 13330}}\times 100 = 1.2\%$	Yanta and Smith (1973)
Averag. process and amplitude effect (σ_{oth})	5% (high turbulence)	5% (high turbulence)	Vafidis (1985)
σ_l	$< 0.1\%$	$< 0.1\%$	
σ_g	—	$< 0.1\%$	Durst et al. (1981)

the subscripts vel, T, g, I and *oth* stand for the accurate variance, turbulence, mean velocity gradient, instrument broadening and other contributions. In Eq. (3) the root-sum-square combination is used to calculate the total precision error from the precision errors of the various contributions.

For the mean velocity the total uncertainty ΔU is affected by both a precision error Δu and a bias error ΔP which is again combined by the root-sum-square rule

$$\Delta U = \sqrt{\Delta u^2 + \Delta P^2}. \tag{4}$$

For the 360° ensemble-averaged measurements taken far from the impeller the maximum uncertainty of the mean velocity was assessed to be less than 2.4% at a 95% uncertainty level, assuming a 100% turbulence intensity, whereas for the turbulent velocities a maximum value of 5.1% was found. In the near-impeller region the uncertainty was higher because of the smaller sample size and the extra contribution of the velocity gradient broadening. For the mean and rms velocities at a 100% turbulence intensity the maximum uncertainties were less than 5.3% and 5.6% respectively, at a 95% confidence level. Details of this analysis are found in Tables 2 and 3.

The positional uncertainty of the measuring volume was limited by the control volume size, the resolution of the traversing table (± 10 and ± 20 μm in the vertical and horizontal directions, respectively) and the visual method used to locate the control volume inside the vessel. This was the major limiting factor, which together with the size of the measuring volume accounted for a maximum uncertainty of ± 100 μm in the vertical direction. In the horizontal plane the maximum uncertainties were of ± 1000 and ± 100 μm when traversing in the azimuthal and radial directions, respectively.

3. Results and discussion

Pinho et al. (1997) have shown that below a Reynolds number of 200 the flow is laminar and the power number ($Ne = P/\rho N^3 D^5$) varies inversely with the Reynolds number ($\mathrm{Re} = \rho N D^2/\mu$), levelling towards a constant value of 0.9 for Reynolds numbers above 1000–2000. The flow characteristics presented below are well within the turbulent regime, as they were measured at a Reynolds number of 50,000. This flow condition is relevant in waste water treatment applications due to the large size of the impeller and in spite of its low rotational speed. In the above definitions of power and Reynolds numbers P, ρ, μ, N and D stand for the power, fluid density, fluid dynamic viscosity, impeller rotational speed and impeller diameter, all in S.I. units except for N which is in [rps].

The co-ordinate system used to present data is schematically shown in Fig. 1 and all the LDA measurements were carried out in the mid-plane between two baffles.

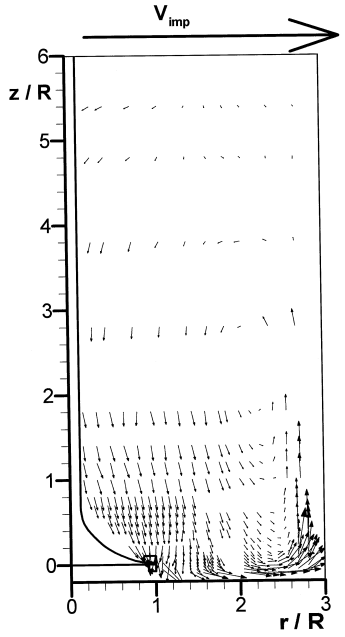

Fig. 2. Vector plot of the radial- axial mean velocity vector in the vertical diametrical plane, in the middle plane between two baffles.

The flow in a mechanically-agitated vessel is usually characterised by two regions: close to the impeller the flow is periodic because it is directly affected by the passage of the blades or ribs, hence its proper characterisation requires angle resolved measurements. Outside this near-impeller region the periodicity has been smeared by the turbulent flow and 360° ensemble-averaging can be correctly used.

The mean flow characteristics of the angle-independent region far from the impeller are presented first and will be followed by a discussion of the extension of the region exhibiting flow periodicity (near-impeller region) and the presentation of the angle-resolved information. Then, the turbulent flow characteristics are presented in the same order. Velocity values are normalised by the impeller tip velocity and the values of the radial and axial locations are normalised by the impeller radius.

3.1. *Mean flow*: *Ensemble- and weighted-average measurements*

The flow discharge from a hyperboloid impeller is radial and this jet is located below the base plane of the impeller as was previously observed by Nouri and Whitelaw (1994) in their measurements with a larger clearance of $C/T = \frac{1}{3}$ and by Ismailov et al. (1997) for $C/T = \frac{1}{30}$. In the present work the impeller is positioned near the bottom of the vessel, also at $C/T = \frac{1}{30}$, and the radial jet flows along the bottom wall as is shown in the vector plot of Fig. 2. This vector plot contains 360° ensemble-average values far from the impeller and weighted average values in the near-impeller region. It can be seen that near the tip of the impeller, vectors are pointing downwards, towards the bottom of the impeller instead of radially, an indication that the discharge from the impeller splits into two streams. Ismailov et al. (1997) have called this a λ-type of flow pattern with the main discharge along the right arm of the λ. The bottom radial jet turns upwards at the vessel side wall and returns radially towards the centre at $z/R \geqslant 2.8$ before descending to the impeller region in the centre of the vessel. Fig. 2 shows that the small clearance of this configuration leads to an overall flow pattern which is proper of an axial flow turbine in spite of the radial-like features of the hyperboloid impeller. We emphasise the similarity with the mean flow pattern of Ismailov et al. (1997), which indicates that the presence of the shear ribs in our work does not seem to have a significant effect upon the mean flow field.

Figs. 3 and 4 present radial profiles of the mean axial, radial and tangential velocity components at regions where the flow was found to be angle-dependent and angle-independent, respectively. The near-impeller profiles were calculated as weighted-averages of the 1° angle-resolved measurements as defined by Eq. (1), and far from the impeller we present the measured 360° ensemble-average data. The descending axial flow at the centre of the vessel has an average magnitude of about 5% of the tip velocity and occupies over 70% of the radius of the vessel whereas the upwards vessel wall jet has a width of about one sixth the tank radius and a maximum magnitude of 15% of the tip velocity. Near the tip of the impeller the high velocities show that the flow is very intense because it is being pushed directly by the ribs.

A radial velocity component is acquired only in the near vicinity of the impeller surface and especially at the bottom of the vessel. The slow motion of the fluid towards the shaft at $4.0 > z/R > 2.8$ has a magnitude of 2% of the tip velocity. At the upper quarter of the vessel ($z/R \geqslant 4.8$) the flow is very weak but still it is possible to discern a radial flow towards the shaft for $r/R < 1.5$ and a radial outwards flow for $r/R > 1.5$ which, together with the axial velocity information indicates the presence of a second weak clockwise vortex not easily observed in the vector plot of Fig. 2. Down, between $z/R = +0.4$ and $+1.8$ the outwards radial flow has a magnitude of about 2% of the tip velocity. At the bottom radial jet, mean velocities are higher than above, reaching maximum values of about 10% of the tip velocity and at the impeller, where the fluid is being pushed by the transport ribs, local mean radial velocities go up to 20–30% of the tip velocity. The main anticlockwise vortex, defined by the circulating flow pattern just described, is centred at around $r/R = 2.4$ and $z/R = 1.75$.

The mean tangential velocity component has magnitudes similar to the mean radial velocity component except near the impeller. Far from the agitator

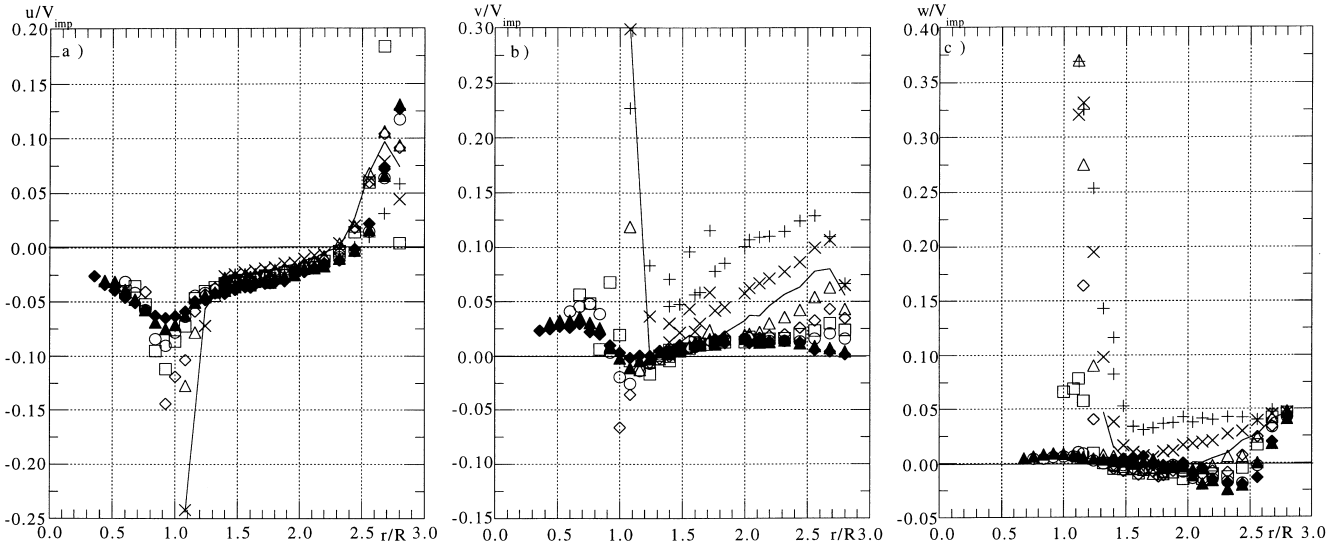

Fig. 3. Radial profiles of the normalised mean axial (u), radial (v) and tangential (w) velocity components at different heights in the vicinity of the impeller. + $z/R = -0.1$, × $z/R = -0.06$, —— $z/R = -0.02$, △ $z/R = +0.02$, ◇ $z/R = +0.06$, □ $z/R = +0.1$, ○ $z/R = +0.14$, ▲ $z/R = +0.22$, ◆ $z/R = +0.30$.

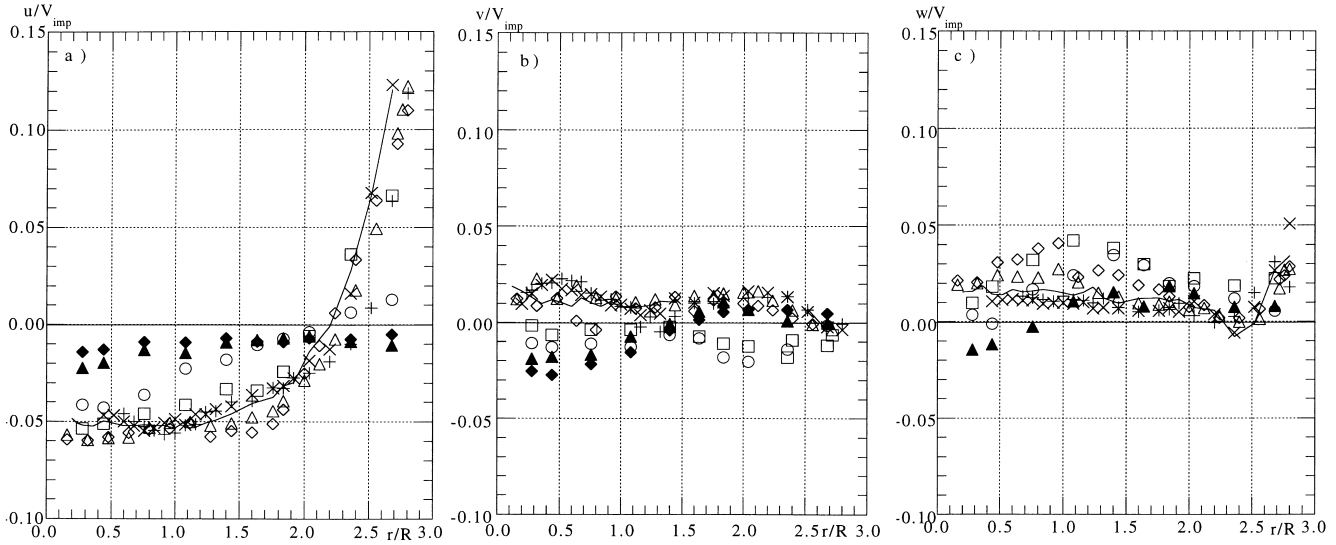

Fig. 4. Radial profiles of the normalised mean axial (u), radial (v) and tangential (w) velocity components at different heights far from the impeller. + $z/R = +0.4$, × $z/R = +0.5$, —— $z/R = +0.8$, △ $z/R = +1.2$, ◇ $z/R = +1.8$, □ $z/R = +2.8$, ○ $z/R = +3.8$, ▲ $z/R = +4.8$, ◆ $z/R = +5.4$.

($z/R \geqslant 0.4$) the fluid slowly rotates in the same direction as the impeller (positive w velocities), with magnitudes between 1 and 4% of the tip velocity. Below the impeller the fluid rotation is also positive and the rotational velocities are higher because of the influence of the transport ribs, but they decrease very quickly with the radius, dropping from over 40% of the tip velocity at $r/R = 1.08$ to less than 10% at $r/R = 1.4$. Just above the impeller base-plane ($z/R = 0$) up to about $z/R = 0.3$–0.4 the fluid rotates with the impeller for $r/R < 1.5$ and in the opposite direction for $1.5 < r/R < 2.5$ with a normalised velocity of 2.5%. In the wall jet region ($r/R > 2.5$) the fluid rotates again in the same direction as the hyperboloid. The counter-rotating flow could be due to the simultaneous influence of the baffles, which act against rotation, and a low-pressure region created by the high-speed jet at the bottom.

3.2. Extent of periodic flow

The periodic flow in the near-impeller region is affected by the eight transport ribs, with the 24 shear ribs having an influence which is limited to the region below the impeller. However, due to the small size of the ribs

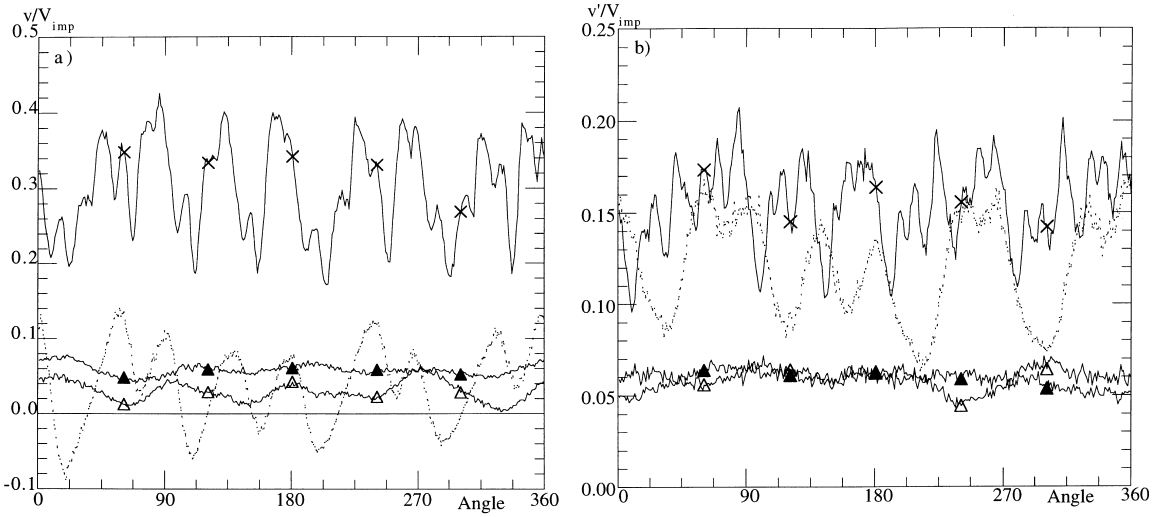

Fig. 5. (a) and (b) Mean and rms radial velocity component at $z/R = -0.06$ as a function of the angular position and at radial locations: $r/R = 1.08$ -X-, $r/R = 1.24$ - - - -, $r/R = 1.4$ -△- and $r/R = 1.76$ -▲-.

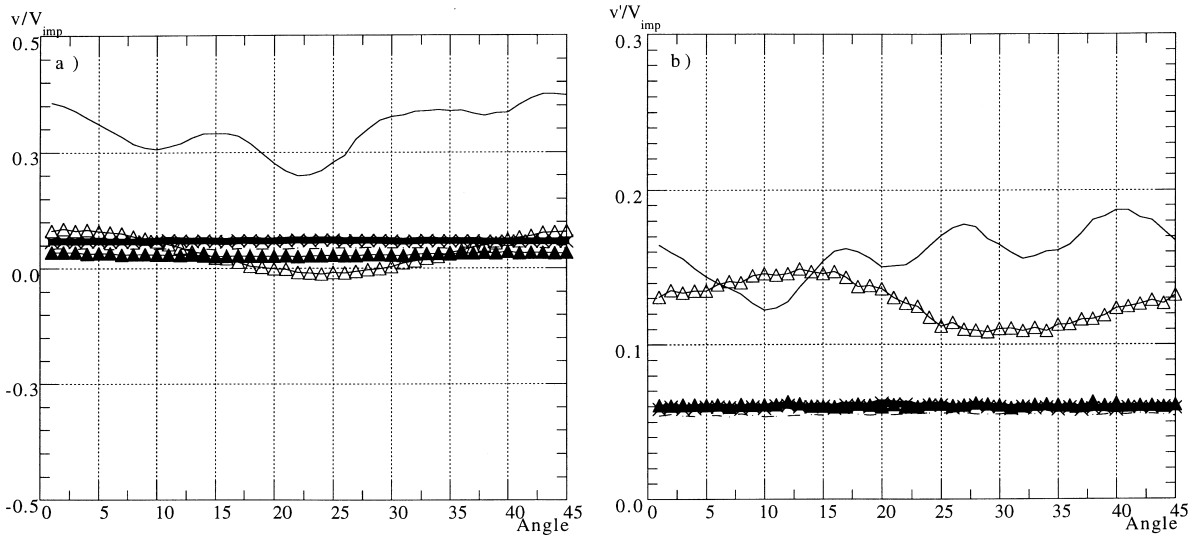

Fig. 6. (a) and (b) Mean and rms radial velocity component at $r/R = 1.08$ (—), $r/R = 1.24$ (△), $r/R = 1.4$ (▲), $r/R = 1.6$ (- - - -) and $r/R = 1.76$ (X) as a function of the angular position at $z/R = -0.06$.

both effects are considerably smaller than usually encountered with conventional agitators which have larger blades.

Near the impeller base-plane and in the bottom wall jet, the periodicity in both mean and turbulent quantities becomes very small for $r/R \geqslant 1.8$ as can be seen in Fig. 5 where various angular profiles of the 1° angle-resolved mean and rms of the radial velocity component are shown at different radial locations and constant $z/R = -0.06$.

The oscillations in the $r/R = 1.76$ profiles of Fig. 5 are of small amplitude and result from two effects: the small sample size of the 1° angle-resolved measurements in such a high turbulent flow and the low amplitude wobbling of the impeller to be discussed later. The corresponding angular profiles of the 45°-average cycle, made from the 1° angle-resolved data, are presented in Fig. 6 and here the extent of periodic flow is limited to $r/R = 1.4$. Note also that very close to the impeller, at $r/R = 1.08$, there are three velocity maxima (24 maxima over the full 360°) corresponding to the effect of the 24 shear ribs, but these are absent at $r/R = 1.24$ where only the transport rib effect remains.

Going upwards from the impeller base-plane sees a reduction in periodicity since one moves into a region where the fluid is being sucked into the impeller region.

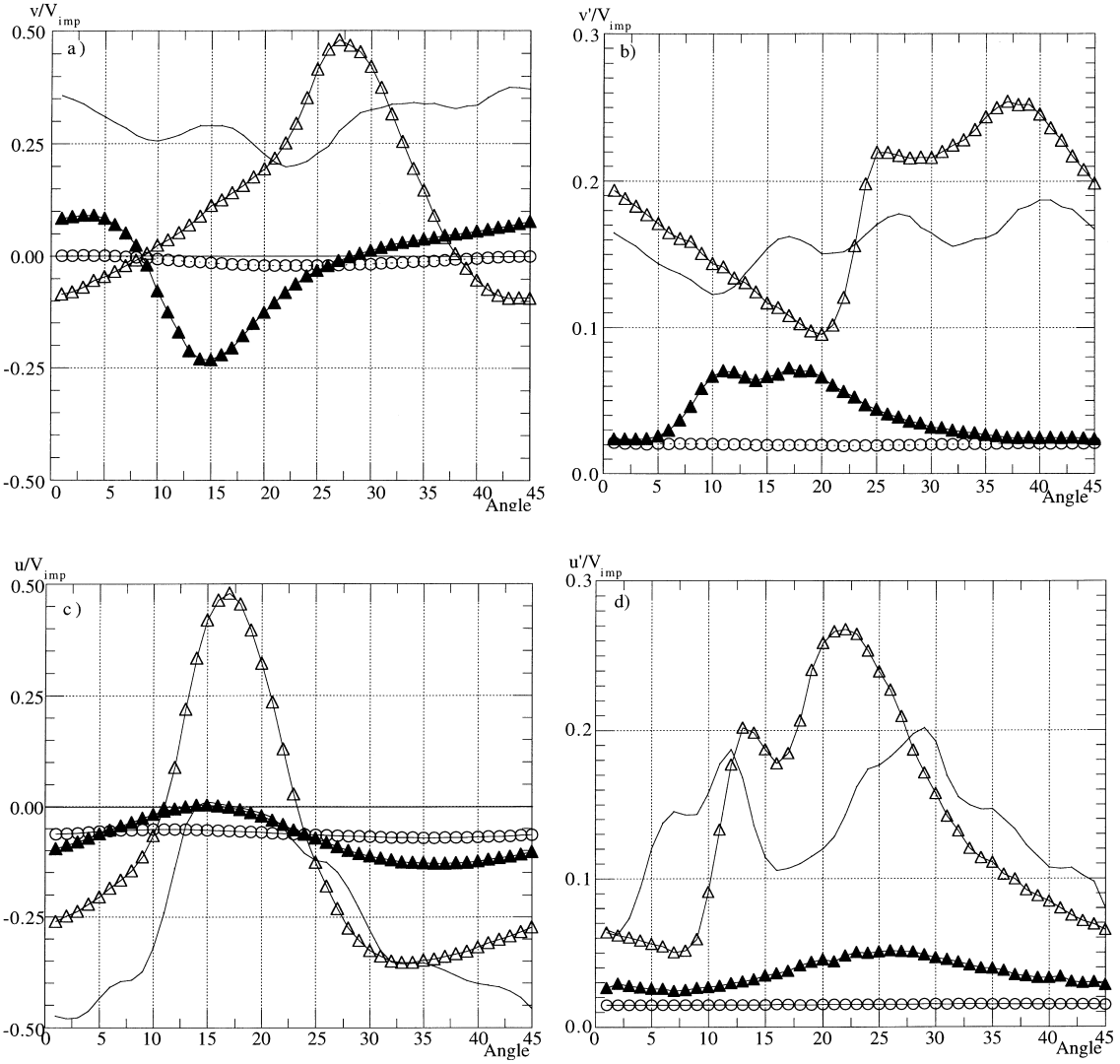

Fig. 7. Angular profiles of the mean radial (a), rms radial (b), mean axial (c) and rms axial (d) velocity components at $z/R = -0.06$ (——), $z/R = +0.02$ (△), $z/R = +0.1$ (▲) and $z/R = +0.22$ (○), for a constant $r/R = 1.08$.

This is clearly shown in the angular profiles of the angle-resolved radial and axial velocity components of Fig. 7: here the radial position is kept constant at $r/R = 1.08$ and the axial position varies from $z/R = -0.06$ to 0.22, where the flow periodicity becomes negligible. The effect of increased radius at constant $z/R = +0.1$, i.e. above the impeller base plane, is plotted in Fig. 8 which shows angular profiles of the 45°-average cycle; here the flow is weakly dependent of angle at $r/R = 1.24$ and steady at $r/R = 1.4$. This agrees with Ismailov et al. (1997) in that the periodicity is observed from the bottom of the vessel up to a region near the upper edge of the transport ribs. However, later in this work we can be more precise in establishing the upper limit at $z/R = 0.2$.

Moving downwards from $z/R = -0.06$ shows an increase in the size of the angle-dependent region because of the λ-shape of the mean flow pattern. Due to difficulties in measuring close to the bottom of the vessel, detailed velocity measurements are scarcer in this region. At the lowest measured horizontal plane ($z/R = -0.1$) there is an increase in the magnitude of the radial velocity with the radius, which suggests that closer to the bottom ($z/R < -0.1$) the radial velocities could be even higher, with a boundary-layer type flow growing towards the side wall.

Similar plots to those just shown are presented in Fig. 9 for $z/R = -0.1$: at $r/R = -1.08$ the periodic effect of the shear ribs is more intense than above, at $z/R = -0.06$ (cf. Fig. 6). Also remarkable is that at $r/R = 1.4$ the angular dependence is very weak, because this location is still outside the right arm of the λ flow pattern, i.e., outside the direct influence of the jet emanating from the impeller surface. Thus, to observe a radial extension of the near-impeller region one must move further down to catch the radial jet.

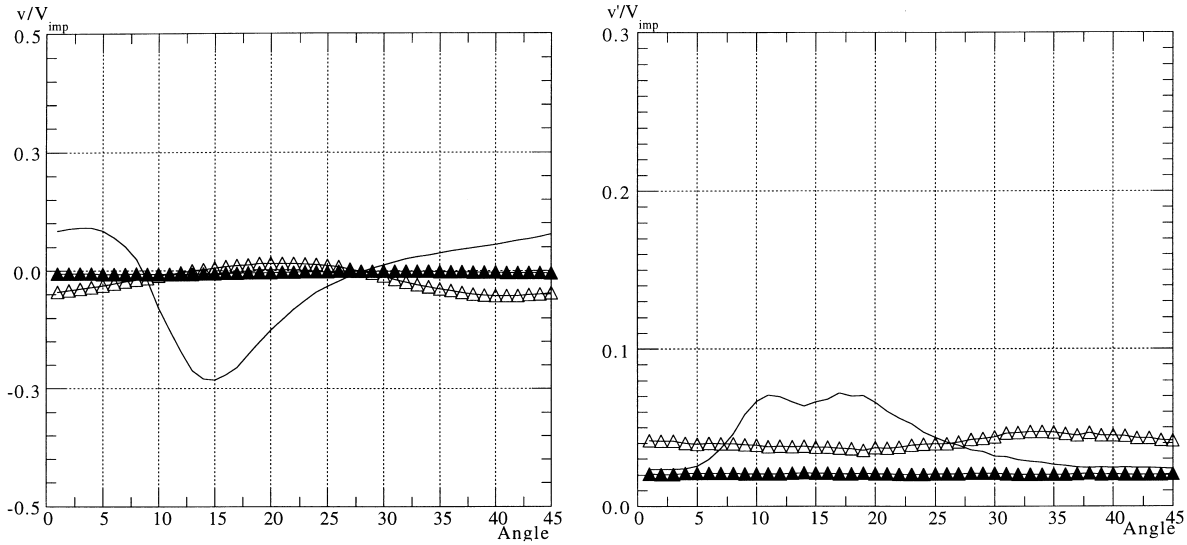

Fig. 8. (a) and (b) Mean and rms radial velocity component at $r/R = 1.08$ (– –), $r/R = 1.24$ (△) and $r/R = 1.4$ (▲) as a function of the angular position at $z/R = +0.1$.

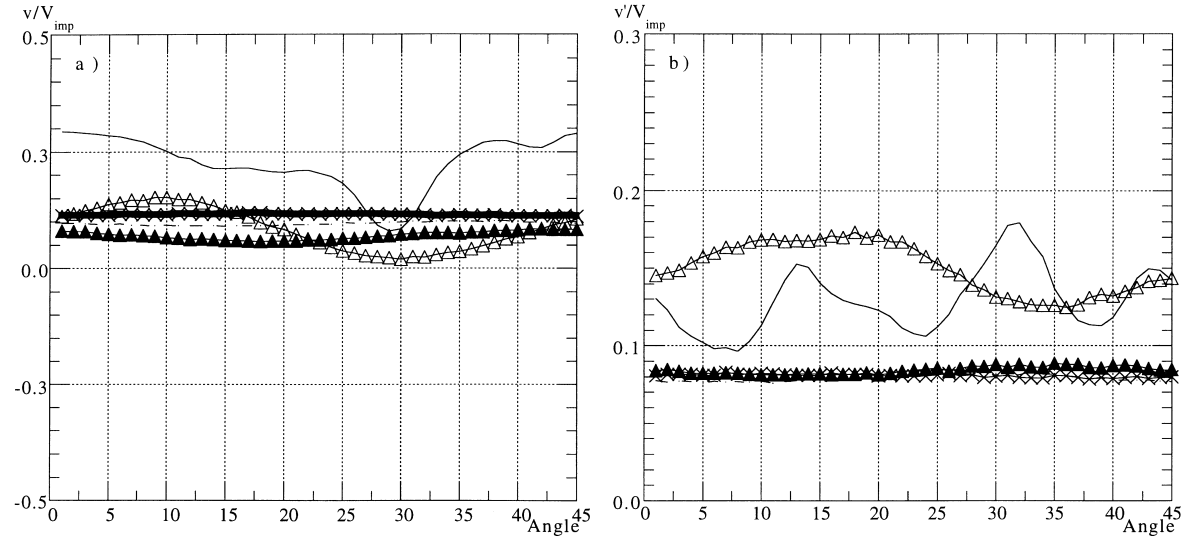

Fig. 9. (a) and (b) Mean and rms radial velocity component at $r/R = 1.08$ (—), $r/R = 1.24$ (△), $r/R = 1.4$ (▲), $r/R = 1.6$ (- - - -) and $r/R = 1.76$ (X) as a function of the angular position at $z/R = -0.1$.

In the whole set of figures just discussed (Figs. 5–9) one identifies three different flow patterns as far as flow periodicity is concerned. This corresponds to three different regions, one below the impeller base plane and two above it. Below the impeller base plane the flow is affected by both the eight transport ribs and the 24 shear ribs, with this combination imparting a low amplitude 24 cycle periodicity which does not spread much outside, as the $r/R = +1.08$ profiles in Figs. 6 and 9 show. Actually the 24 cycles are well identified in the rms profiles and not so in the mean which shows a less changeable shape, since the eight major cycles are disturbed by the strong tangential flow created by the 24 shear ribs, which tend to smooth out the periodicity imposed by the transport ribs. Since the flow discharging from the impeller descends towards the bottom wall along the right arm of the λ flow pattern, moving radially away from the impeller reduces the magnitude of the "noise" produced by the transport ribs as can be confirmed by comparison with the angular profile at $r/R = +1.24$, which shows better the eight cycle periodicity.

The reduction of the flow periodicity occurs through a pairing process which leads to the formation of only four low-amplitude cycles over 360° at $r/R = 1.4$. The curves pertaining to $r/R = 1.08$ and 1.24 are also seen to decay on the average to values of about 5% of the tip

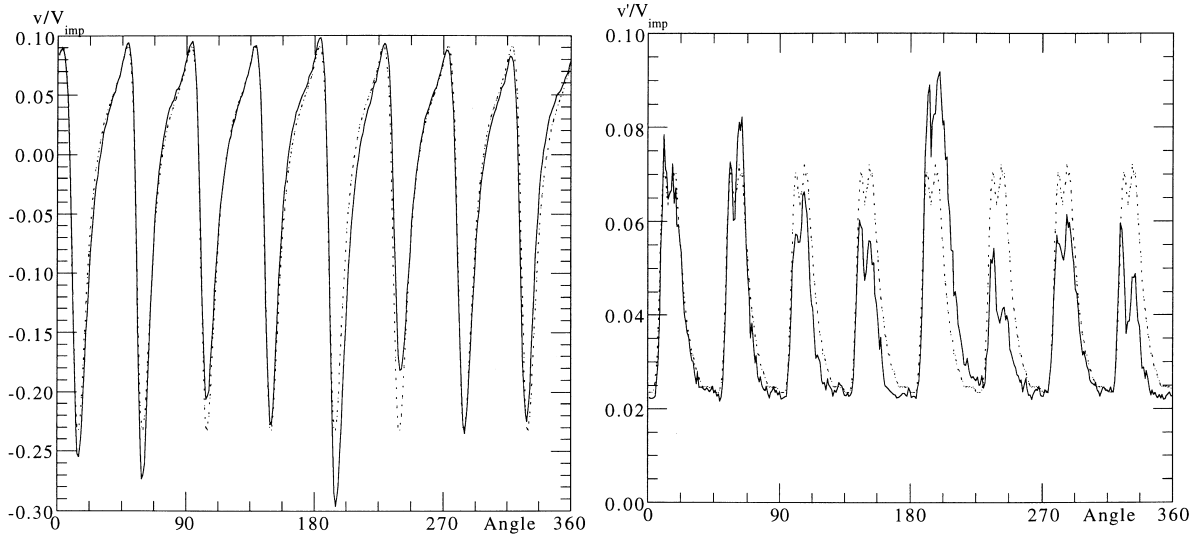

Fig. 10. (a) and (b) Angular profiles of the mean and rms normalised radial velocities at $z/R = +0.1$ and $r/R = 1.08$. Solid line: measured profile. Broken line: calculated average cycle.

velocity as we move into a zone of stronger axial flow. At a higher radius ($r/R \geqslant 1.4$) the periodicity has been reduced to a weak single cycle, an effect which we attribute to the small wobbling of the impeller. This behaviour contrasts to that found by Ismailov et al. (1997) for impellers without shear ribs where only an 8-cycle periodicity is observed.

Above the impeller base plane, at the plane touching the upper edge of the shear ribs ($z/R = +0.1$), the flow exhibits a strong eight- cycle periodicity with the observed cycle-to-cycle differences always taking place at the same location, as seen in the 360° angular profile of Fig. 10. This suggests imperfections in the positioning of the ribs on the impeller upper surface. The eight measured cycles were averaged into the usual single 45° cycle and this average profile, also shown in Fig. 8, is reproduced as a dashed line to the full 360° in Fig. 10, to help assess the magnitude of the cycle-to-cycle variations. These differences are larger in the fifth and sixth cycle and in the rms of the velocity than in the mean velocity being at most of 30% and 20% in magnitude, respectively. The stronger effect upon the rms is expected, because of its strong dependence of the shear rate values. Since the gradients of the mean velocities are large, slight imperfections in the construction change the maximum shear rate and thus the value of the rms of the velocity.

Close inspection of the impeller showed that the 6th transport rib, located at 225°, was slightly bent forward rather than being perpendicular to the impeller surface and could be responsible for the two different cycles which stand between 180° and 270°. The gentle wobble of the impeller motion and other minor imperfections could then be responsible for the other smaller variations since the manufacturer of the impeller used a manual process to fix the ribs to the impeller surface.

3.3. Mean flow: angle-resolved measurements in the near-impeller field

Fig. 11 shows vector plots of the radial-axial mean velocity vector as 1° angle-resolved measurements at four equally spaced angular planes (11°, 22°, 34° and 45°) between two consecutive transport ribs. The impeller is rotating from the plane of the paper towards the reader. Two features are clear from these figures: the flow discharge from the tip of the impeller separates into the two streams that form the two legs of the λ-type flow, and in the first half of the cycle there is a reversed flow between the transport ribs on the upper surface of the impeller (cf. Fig. 11a). The sequence of figures suggests that a small intense vortex is emanating from the tip of the transport ribs, but a better assessment would require more detailed measurements with a LDA system with a smaller control volume.

The λ-shaped mean flow pattern was also observed in the impeller with no shear ribs by Ismailov et al. (1997), but it looks weaker in the present work because it is difficult to discern in the weighted-average plots, although this could be attributed to measuring difficulties below the impeller.

The reversal of the flow at the upper surface was noticed before by Piqueiro et al. (1996) and is due to the wake behind the transport ribs as it is more evident in the 11° and 22° planes, but not so at 34°.

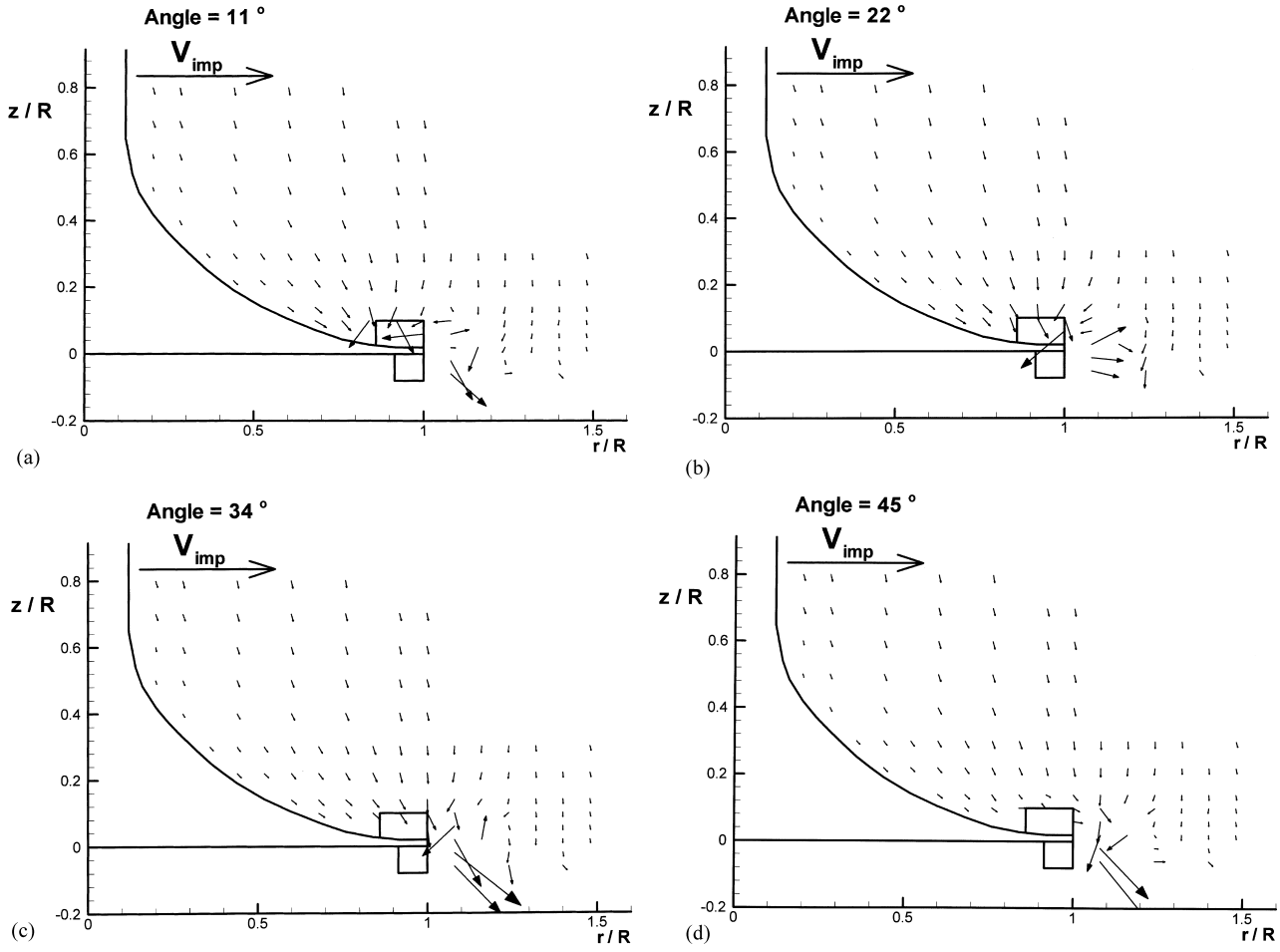

Fig. 11. Vector plots of the radial- axial mean velocity components in the vertical diametrical plane at 11°, 22°, 34° and 45°.

The vector plots confirm the limited extent of the near-impeller region: here we can observe that the on-coming flow above the transport ribs at $z/R = 0.2$ is weakly affected by the rib passage.

3.4. *Turbulent flow*: *ensemble- and weighted-average measurements*

Figs. 12 and 13 represent radial profiles of the normalised rms of the axial, radial and tangential velocity components at different heights. As with the mean velocities in the near-impeller region the profiles were made from weighted-averages as defined in Eq. (2) and from the 360° ensemble-average for data taken far from the impeller.

Two different zones are distinguished: above $z/R = +0.14$ the turbulence is isotropic and remains fairly constant at about 2% of the tip velocity in the centre of the vessel, growing to 4% near the side walls regardless of the vessel height. The higher turbulence on the side wall region is due to turbulence production in the side wall jet plus a contribution of advected turbulence coming from the high turbulent radial flow at the bottom of the vessel. Near the free surface, the almost stagnant fluid reduces the turbulence to values of about 1–1.5% of the tip velocity.

Below $z/R = +0.14$ the turbulence continues to be rather isotropic, but reaches higher values because of the proximity of the impeller and of the bottom of the vessel. In the near-impeller region the high shear rates created by the passage of the shear and transport ribs have important contributions to the production of turbulence, whereas at the bottom of the vessel the turbulence is produced at the boundary layer created by the radial discharge jet. An assessment of the real turbulence near the impeller is made in the next section from the data pertaining to the angle-resolved measurements. Another region of local high turbulence is along the side walls of the vessel where there is also turbulence production at the boundary layer.

Elsewhere the turbulence was isotropic and in most of the bulk of the vessel the normalised kinetic energy k/V_{tip}^2 remained fairly constant at a low 0.06%.

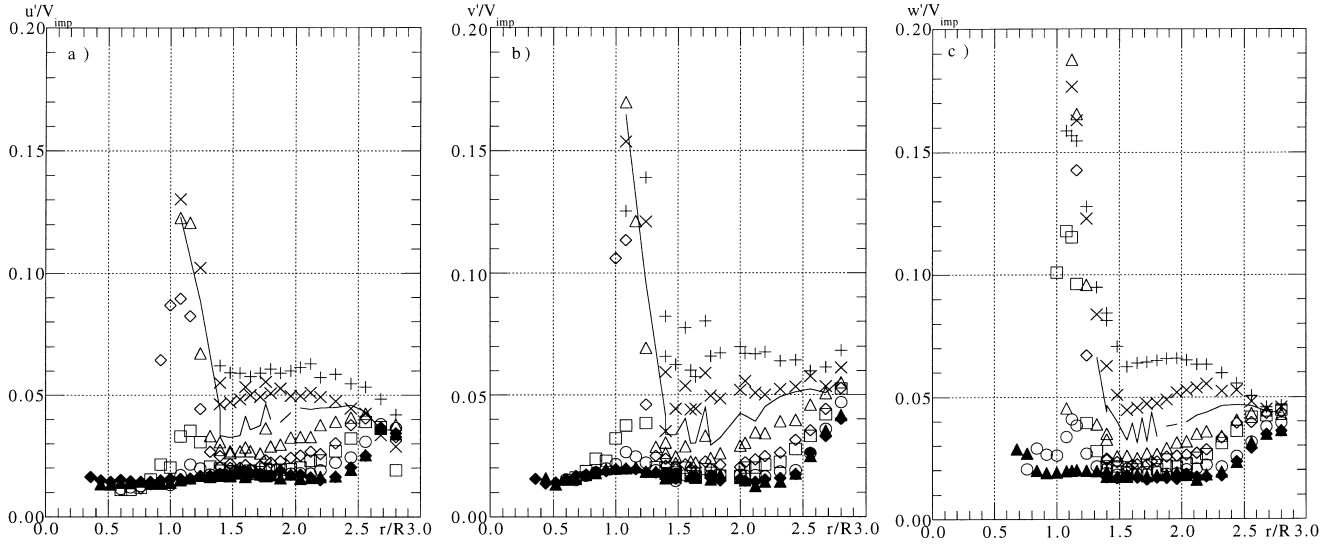

Fig. 12. Radial profiles of the normalised rms axial (u), radial (v) and tangential (w) velocity components at different heights in the vicinity of the impeller. + $z/R = -0.1$, × $z/R = -0.06$, —— $z/R = -0.02$, △ $z/R = +0.02$, ◇ $z/R = +0.06$, □ $z/R = +0.1$, ○ $z/R = +0.14$, ▲ $z/R = +0.22$, ◆ $z/R = +0.30$.

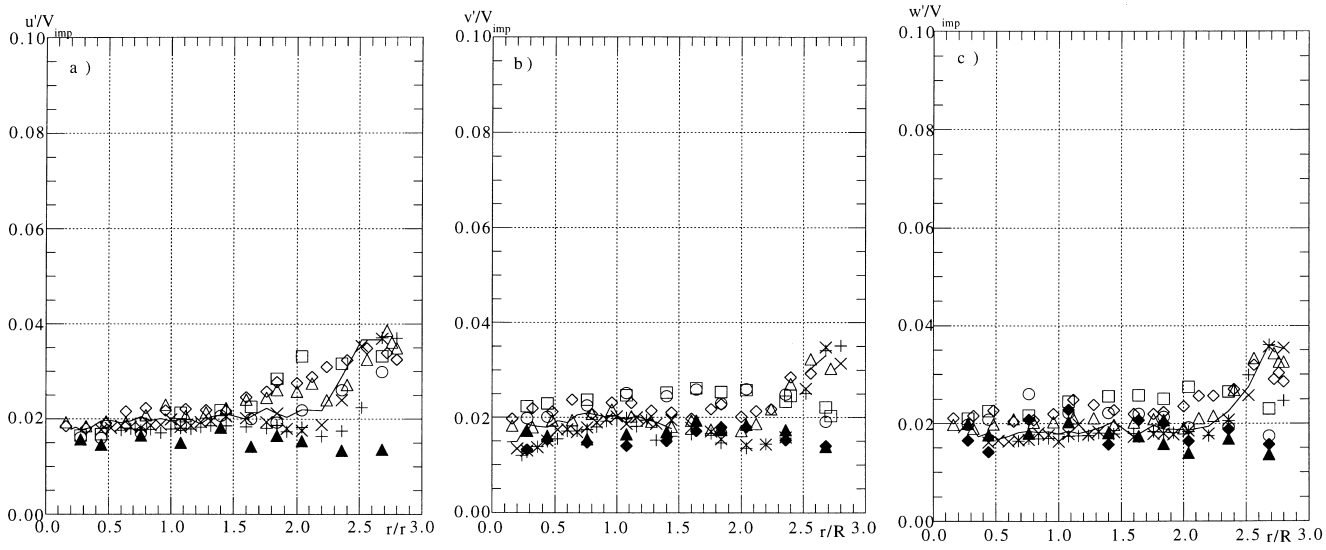

Fig. 13. Radial profiles of the normalised rms axial (u), radial (v) and tangential (w) velocity components at different heights far from the impeller. + $z/R = +0.4$, × $z/R = +0.5$, —— $z/R = +0.8$, △ $z/R = +1.2$, ◇ $z/R = +1.8$, □ $z/R = +2.8$, ○ $z/R = +3.8$, ▲ $z/R = +4.8$, ◆ $z/R = +5.4$.

3.5. Turbulent flow: Angle-resolved measurements in the near-impeller region

Near the ribs of the impeller the turbulence is not isotropic and depends of the angular position, as can be seen in the profiles of normalised axial, radial and tangential normal Reynolds stresses of Figs. 14 and 15. In Fig. 14 angular profiles are shown at a constant radial distance of $r/R = 1.08$, i.e. near the tip of the hyperboloid, for various axial locations below ($z/R < 0$) and above ($z/R > 0$) the impeller base plane, whereas for Fig. 15 z/R is kept constant at $+0.02$ and the radius is varied between $r/R = 1.08$ and 1.24. In both figures, an angular range of 45°, corresponding to the average cycle imposed by the transport ribs, is plotted.

The tangential turbulence is the most visibly affected by the presence of the shear ribs fixed at the bottom surface of the impeller with three cycles evident at profiles for z/R in Fig. 14c). The other two components of turbulence are also influenced by the shear ribs since the

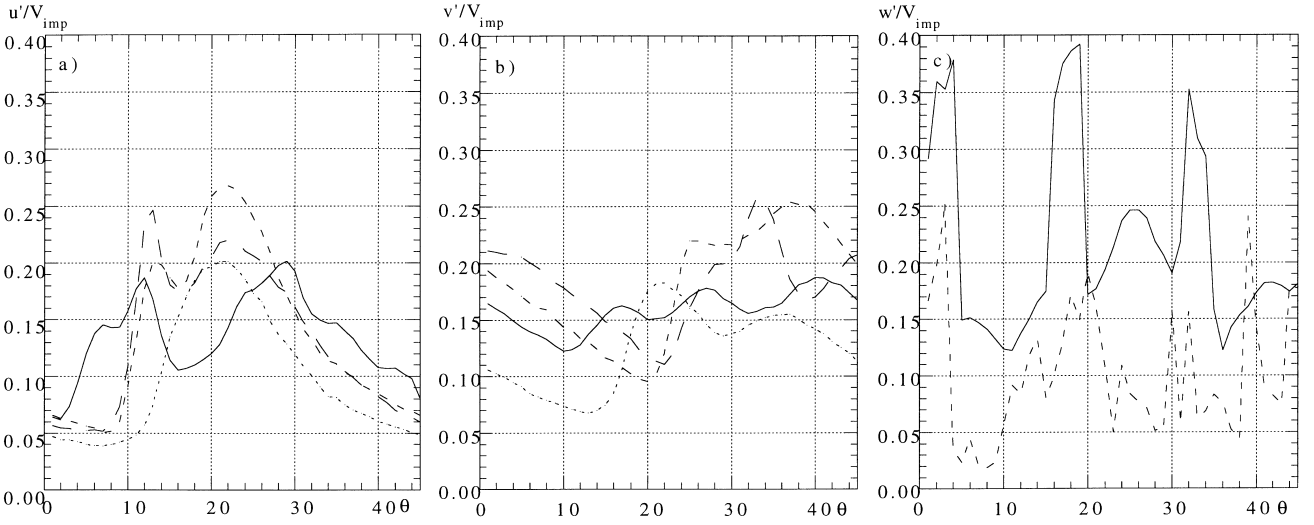

Fig. 14. Angular profiles of u'/V_{imp} (a), v'/V_{imp} (b) and w'/V_{imp} (c) for $r/R = 1.08$ and at different heights: full line $z/R = -0.06$; decreasing dash length $z/R = -0.02, +0.02$ and $+0.06$.

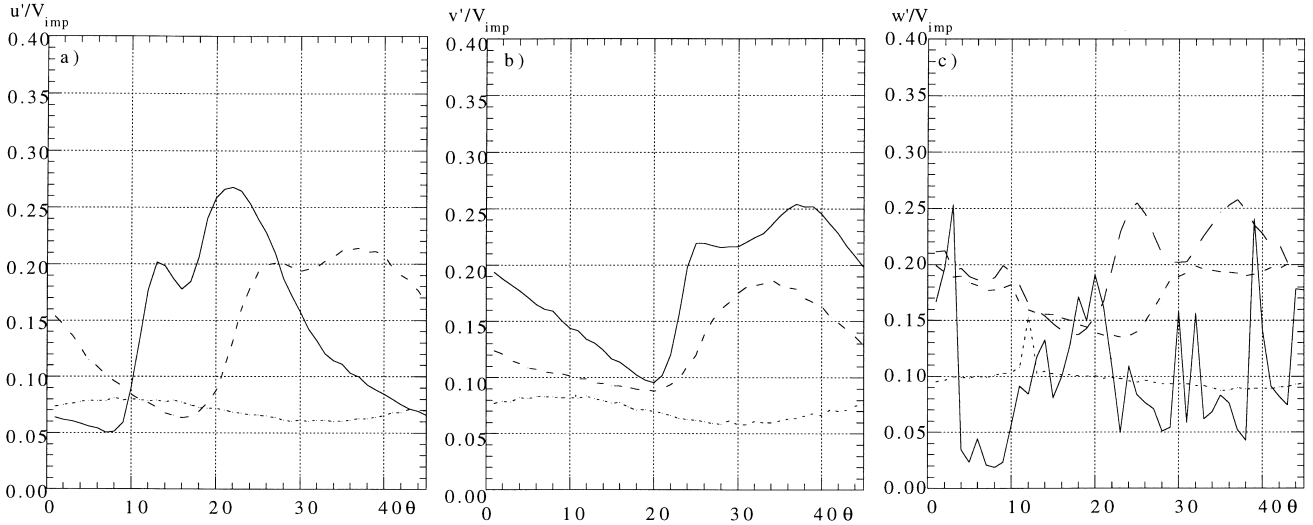

Fig. 15. Angular profiles of u'/V_{imp} (a), v'/V_{imp} (b) and w'/V_{imp} (c) for $z/R = +0.02$ and at different radial locations: full line $r/R = 1.08$; decreasing dash length $r/R = 1.12$, 1.16 and 1.24.

maximum turbulence kinetic energy is 65% higher than that reported by Ismailov et al. (1997) for the hyperboloid without shear ribs.

Figs. 14 and 15, together with contour plots of the normalised Reynolds stresses, one of which is shown here in Fig. 16 for an angle of 34°, show the tangential turbulence to have the highest values followed by the radial and axial components, both very similar in magnitude but initially out-of-phase (compare Fig. 14a with Fig. 14b). In the contour plots of Fig. 16 the impeller also rotates from the plane of the paper towards the reader.

On moving away from the impeller the axial and radial turbulence components become in-phase with the maximum turbulence reaching the highest values in the last quarter of the way between consecutive transport ribs, i.e. between 30 and 40° well represented by the behaviour at 34°. The tangential component of turbulence reaches the highest values, but also the widest spatial influence, also in the last quarter of the way between consecutive transport ribs as is so well shown in the contour plot of Fig. 16c). Maximum values of velocity fluctuations occur just after the fluid leaves the impeller and along the right arm of the λ-shaped jet emanating from the impeller and are of 0.071, 0.063 and 0.15 for u'^2/V_{imp}^2, v'^2/V_{imp}^2 and w'^2/V_{imp}^2, respectively. The corresponding maximum turbulence kinetic energy k is of about 9.5% of V_{imp}^2 which represents an increase of 65% over that reported for the hyperboloid impeller without shear ribs, as mentioned

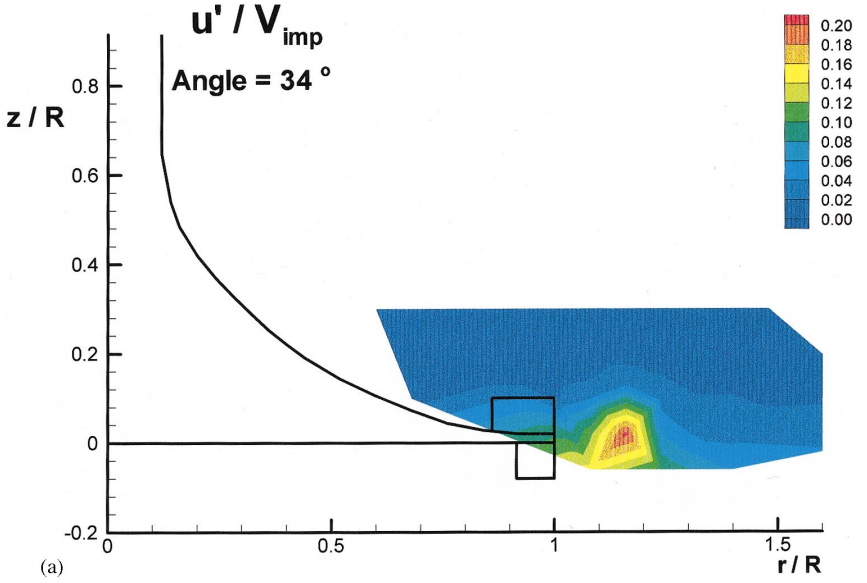
u' / V imp
Angle = 34 °
z / R
r / R
0.20
0.18
0.16
0.14
0.12
0.10
0.08
0.06
0.04
0.02
0.00
0.8
0.6
0.4
0.2
0
-0.2
0
0.5
1
1.5

(a)

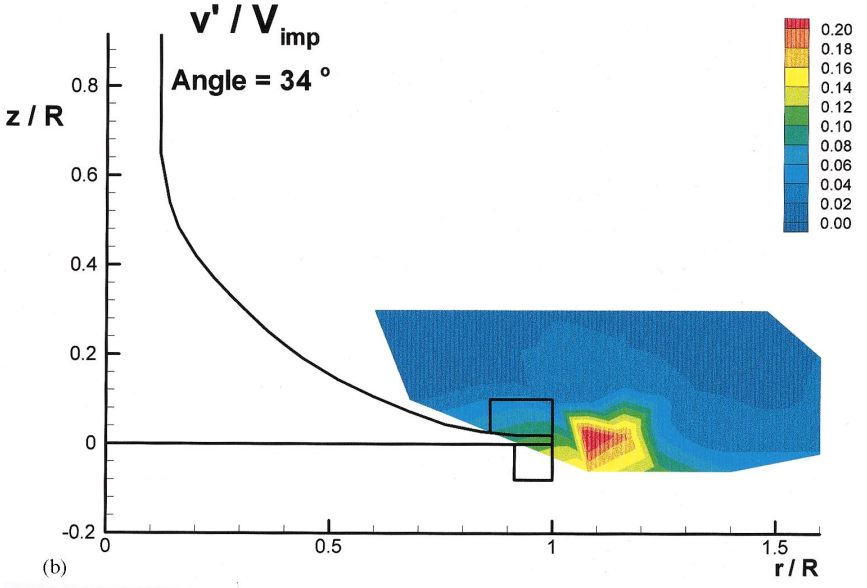
v' / V imp
Angle = 34 °
z / R
r / R
0.20
0.18
0.16
0.14
0.12
0.10
0.08
0.06
0.04
0.02
0.00
0.8
0.6
0.4
0.2
0
-0.2
0
0.5
1
1.5

(b)

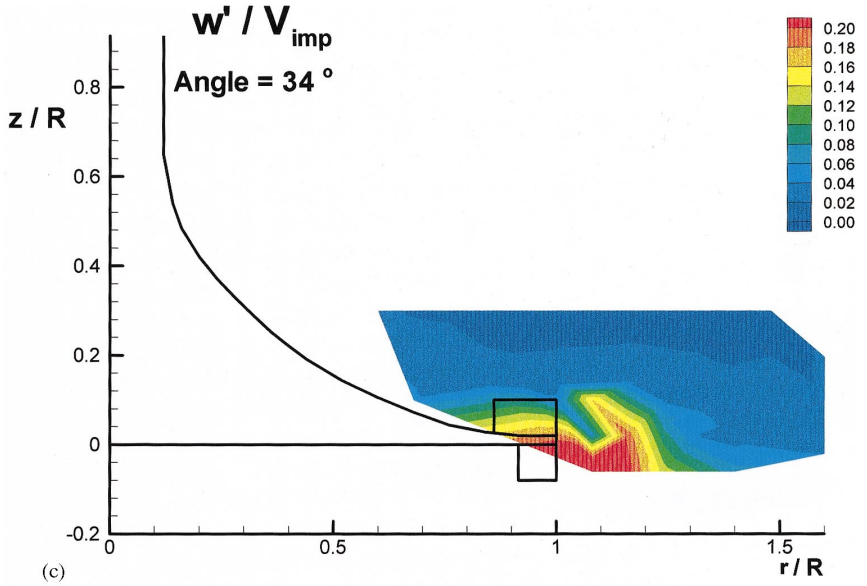
w' / V imp
Angle = 34 °
z / R
r / R
0.20
0.18
0.16
0.14
0.12
0.10
0.08
0.06
0.04
0.02
0.00
0.8
0.6
0.4
0.2
0
-0.2
0
0.5
1
1.5

(c)

above. Note that the maximum values of the three normal Reynolds stresses do not occur at exactly the same locations.

Below the impeller we were not able to measure the three components of the normal Reynolds stress, but for the tangential component the measured values were lower than those on the right arm of the λ-shaped jet, in spite of the presence of the shear ribs, but naturally higher than those measured by Ismailov et al. (1997) for the agitator without shear ribs.

4. Conclusions

Laser-Doppler anemometry was used to perform detailed angle-resolved measurements of the mean and rms of the three components of the velocity vector in a stirred vessel powered by a low consumption hyperboloid impeller having eight transport ribs and 24 shear ribs on its upper and lower surface, respectively. The measurements were carried out at a Reynolds number of 50,000 for which the power number was equal to 0.9.

The clearance of the impeller was low and thus it contributed to an overall flow pattern typical of that found with axial impellers. The discharge from the hyperboloid was radial following a λ-type pattern, i.e. part of the flow went below the impeller whereas the other part was discharged towards the bottom and outer wall (right arm of λ). In the bulk of the flow the mean velocities were of the order of 5% of the tip velocity, increasing to about 20% V_{tip} towards the tip of the impeller because of the ribs. The small size of the ribs limited the extent of periodic flow to a region bounded by the bottom and $z/R = 0.2$, and extending radially from $r/R = 0.85$–1.4, plus the fluid below the impeller. In the discharge jet the periodic flow was initially characterised by an eight cycle periodicity followed by their full homogenisation by a pairing process as the fluid moved away. Behind each of the eight transport ribs the flow was separated, especially in the first-half of the cycle before the next rib.

In terms of the turbulent flow field, the bulk of the flow is isotropic at about 2% of the tip velocity, growing to 4% as the side wall boundary-layer is approached, and decreasing to 1–1.5% of V_{tip} near the free-surface. Below $z/R = +0.14$ the turbulence remains isotropic but reaches higher values due to the proximity of the impeller and of the bottom boundary layer.

The highest turbulence was encountered on the right arm of the λ-shaped impeller discharge stream with values of the maximum turbulent kinetic energy of 9.5% of V_{tip}^2. In this region the tangential turbulence was the highest, followed by the axial and the radial components. Maximum values of these components, normalised by V_{tip}^2, were 0.15, 0.071 and 0.063, respectively. The influence of the shear ribs was not restricted to the region below the impeller but also contributed to the higher turbulence in the right arm of the λ-shaped discharge jet, increasing maximum turbulence by about 65% relative to the non-shear ribbed hyperboloid of Ismailov et al. (1997).

These results indicate that aerators should be totally under the hyperboloid impeller if bubble break-up is to be effective, and that the insertion of additives will be most effective if placed below the impeller or at around $z/R = -0.06$ and $r/R = 1.04$ in order to optimise mixing times.

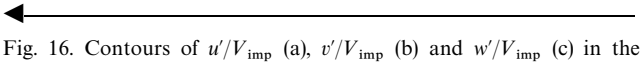

Fig. 16. Contours of u'/V_{imp} (a), v'/V_{imp} (b) and w'/V_{imp} (c) in the vicinity of the impeller, at an angle of 34° between consecutive transport ribs.

Acknowledgements

The authors would like to thank the European Commission and JNICT- Junta Nacional de Investigação Científica, for making possible this work through the contracts number JOU 2- CT9- 0127 and PEAM/C/TAI/265/93, respectively. Special thanks are due to Mr. M. Schäfer, who helped with the set-up and some initial measurements, and to Mr. Jerónimo de Sousa for his technical support. The authors are listed alphabetically.

Appendix A

The weighted-average variance $\overline{u'^2_w}$ defined in Eq. (2), and based on 1° angle-resolved variance values $\overline{u'^2_\theta}$, was preferred to the total ensemble-average variance $\overline{u'^2}$ defined as

$$\overline{u'^2} \equiv \frac{\sum_{i=1}^{N}(u_i - \bar{u})^2}{N}, \tag{A.1}$$

on the basis that the latter suffered from significant broadening from mean flow periodicity effects. In Eq. (A.1) N represents the total sample size, i.e. the sum of N_θ for θ varying between 1 and 360, and u_i represents the i-ocurrence of an instantaneous velocity. It is possible to relate $\overline{u'^2_w}$ and $\overline{u'^2}$ with a little of algebra.

Using the properties of averaging (A.1) can be rewritten as

$$\overline{u'^2} = \frac{\sum_{i=1}^{N} u_i^2}{N} - \bar{u}^2 \tag{A.2}$$

and similarly for the 1° ensemble-average

$$\overline{u'^2_\theta} \equiv \frac{\sum_{j=1}^{N_\theta}(u_{j,\theta} - \overline{u_\theta})^2}{N_\theta} = \frac{\sum_{j=1}^{N_\theta} u_{j,\theta}^2}{N_\theta} - \bar{u}_\theta^2. \tag{A.3}$$

Table 4
Comparison between the total ensemble- and weighted-average rms values of the axial velocity component

r/R	z/R	$\overline{u'}/V_{\text{imp}}$	$\overline{u'_w}/V_{imp}$
1.08	+ 0.02	0.284	0.145
1.32	+ 0.02	0.0346	0.0344
1.08	+ 0.06	0.1464	0.0988
1.32	+ 0.06	0.0473	0.0463
1.08	− 0.02	0.243	0.136
1.24	− 0.02	0.1027	0.0956
1.08	− 0.06	0.2247	0.1383
1.24	− 0.06	0.1314	0.1113

The sum of the squares of instantaneous velocities in Eq. (A.2) is also the extension over the theta domain of the sum of the squares of the instantaneous θ-velocities, i.e.,

$$\sum_{i=1}^{N} u_i^2 = \sum_{\theta=1}^{360} \sum_{j=1}^{N_\theta} u_{j,\theta}^2, \tag{A.4}$$

which can be solved, after substitution of Eq. (A.3) into Eq. (A.4), as

$$\sum_{i=1}^{N} u_i^2 = \sum_{\theta=1}^{360} N_\theta(\overline{u'^2_\theta} + \bar{u}_\theta^2). \tag{A.5}$$

Therefore, we end up with

$$\overline{u'^2} = \sum_{\theta=1}^{360} \frac{N_\theta(\overline{u'^2_\theta} + \bar{u}_\theta^2)}{\sum_{\theta=1}^{360} N_\theta} - \bar{u}^2. \tag{A.6}$$

Using now the definition of weighted-average variance of Eq. (2) one concludes that

$$\overline{u'^2} = \overline{u'^2_w} + \frac{\sum_{\theta=1}^{360} N_\theta \bar{u}_\theta^2}{N} - \bar{u}^2 = \overline{u'^2_w} + \frac{\sum_{\theta=1}^{360} N_\theta \bar{u}_\theta^2}{N} - \left[\frac{\sum_{\theta=1}^{360} N_\theta \bar{u}_\theta}{N}\right]^2, \tag{A.7}$$

where the equivalence between the weighted-average and the total ensemble-average mean velocities was used. This is so because both quantities are linear combinations of the same instantaneous velocity values.

Eq. (A.7) compares a sum of squares with the square of a sum, further complicated by the sample size distribution effect. For an even distribution of the local sample size N_θ, the total ensemble-average variance will be higher than the weighted-average variance provided the 1° ensemble-average mean velocities have both negative as well as positive values, but will be lower if all 1° ensemble-average mean velocities have the same sign.

In the real case this is not so because the sample size is not at all evenly distributed along the azimuthal direction. Samples are larger where the 1° mean velocity is larger, and not where the local turbulence is higher, and since that means a local higher flow rate there are consequently more scattering particles crossing the control-volume. The distribution of the local sample size N_θ has such a strong effect that it dramatically changes the tendencies discussed in the previous paragraph, and that this is so was confirmed for the three components of velocity at all points in the vicinity of the impeller.

Some of those comparative results are presented in the Table 4 for the axial component of velocity and at a number of representative locations where the flow is highly periodic and the turbulence is anisotropic. The results in Table 4 confirm the over-prediction of the total ensemble-average rms relative to the weighted-average rms and the discrepancy between the two values diminishes as the distance from the impeller increases. For the other two components of velocity exactly the same behaviour was observed.

References

Bakker, A., & van den Akker, H. E. A. (1990). The use of profiled axial flow impellers in gas-liquid reactors. In Proceedings of Fluid Mixing IV. *Institute of Chemical Engineering Symposium Series No.* 121, pp. 153–160.

Buckland, B. C., Gbewonyo, K., DiMasi, D., Hunt, G., Westerfield, G., & Nienow, A. W. (1988). Improved performance in viscous mycelial fermentation by agitator retrofitting. *Biotechnology Bioengineering*, *31*, 737–742.

Coleman, H. W., & Steele, W. G. (1989). *Experimentation and uncertainty analysis for engineers*. New York: Wiley.

Costes, J., & Couderc, J. P. (1988). Influence of the size of the units- II. Spectral analysis and scales of turbulence. *Chemical Engineering Science*, *43*, 2765.

Cutter, L. A. (1966). Flow and turbulence in a stirred tank. *American Institute of Chemical Engineering Journal*, *12*, 35–45.

Durst, F., Melling, A., & Whitelaw, J. H. (1981). *Principles and Practice of Laser-Doppler Anemometry* (2nd Edition). New York: Academic Press.

Höfken, M., Bischof, F., & Durst, F. (1991). Novel hyperboloid stirring and aeration system for biological and chemical reactors. *American Society of Mechanical Engineering-Fluids Engineering Division- Industrial Applications of Fluid Mechanics*, *132*, 47.

Höfken, M. & Bischof, F. (1993). *Hyperboloid stirring and aeration system: Operating principles, application, technical description*. Invent GmbH report, version 1.1, Erlangen.

Höfken, M., Zähringer, K., & Bischof, F. (1994). Stirring and aeration system for the upgrading of small waste water treatment plants. *Water Science and Technology*, *29*, 149.

Ismailov, M., Schäfer, M., Durst, F., & Kuroda, M. (1997). Turbulent flow pattern of hyperboloid stirring reactor. *Journal Chemical Engineering of Japan*, *30*, 1090.

Kresta, S. M., & Wood, P. E. (1993). The flow field produced by a pitched blade turbine: characterisation of the turbulence and estimation of the dissipation rate. *Chemical Engineering Science*, *48*, 1761.

Kusters, K. A. (1991). *The influence of turbulence on aggregation of small particles in agitated vessels*. Ph.D thesis. Technical University of Eindhoven.

Laufhütte, H. D., & Mersmann, A. B. (1985). Dissipation of the power in stirred vessels. *5th European conference on mixing*, Würzburg, West Germany, 10–12 June. Paper, 33, pp. 331–340.

Mujumdar, A. S., Huang, B., Wolf, D., Weber, M. E., & Douglas, W. J. M. (1970). Turbulence parameters in a stirred tank. *Canadian Journal Chemical Engineering*, *48*, 475–483.

Nouri, J. M., & Whitelaw, J. H. (1992). Particle velocity characteristics of dilute to moderately dense suspension flows in stirred reactors. *International Journal Multiphase Flow*, *18*, 21.

Nouri, J. M., & Whitelaw, J. H. (1994). Flow characteristics of hyperboloid stirrers. *Canadian Journal Chemical Engineering*, *72*, 782.

Pinho, F. T., Piqueiro, F. M., Proença, M. F., & Santos, A. M. (1997). Power and mean flow characteristics in mixing vessels agitated by hyperboloid stirrers. *Canadian Journal Chemical Engineering*, *75*, 832.

Piqueiro, F. M., Proença, M. F., Pinho, F. T. & Santos, A. M. (1996). Mean and turbulent flow characteristics of single hyperboloid impeller stirred vessels. *Proceedings 8th international symposium on application of laser techniques to fluid mechanics*, paper 8.3, Lisbon, July.

Reed, X. B., Princz, M., & Hartland, S. (1977). Laser- doppler measurement of turbulence in a standard stirred tank. In Proceedings 2nd European conference mixing, Paper B1, Cambridge, UK, 30 March-1 April 1.

Rutherford, K., Mahmoudi, S. M. S., Lee, K. C., & Yianneskis, M. (1996a). The influence of Rushton impeller blade and disk thickness on the mixing characteristics of stirred vessels. *Transactions of the Institute of Chemical Engineering*, *74*, 369–378.

Rutherford, K., Mahmoudi, S. M. S., Lee, K. C., & Yianneskis, M. (1996b). Hydrodynamic characteristics of dual rushton impeller stirred vessels. *American Institute of Chemical Engineering Journal*, *42*, 332–346.

Schäfer, M., Yianneskis, M., Wächter, P., & Durst, F. (1998). Trailing vortices around a 45° pitched-blade impeller. *American Institute of Chemical Engineering Journal*, *44*, 1223–1246.

T. S. I. (1988). *Manual of the 1990 C counter*. TSI Incorporation, Minneapolis.

Wu, H., & Patterson, G. K. (1989). Laser doppler measurements of turbulent flow parameters in a stirred mixer. *Chemical Engineering Science*, *44*, 2207.

Vafidis, C. (1985). Aerodynamics of reciprocating engines. Ph.D thesis, Imperial College, University of London.

Yianneskis, M., Popiolek, Z., & Whitelaw, J. H. (1987). An experimental study of steady and unsteady flow characteristics of stirred reactors. *Journal Fluid Mechanics*, *175*, 537.

Yanta, W. J., & Smith, R. A. (1973). Measurements of turbulence-transport properties with a laser- doppler velocimeter. 11th aerospace science meeting. *Washington, AIAA paper*, 73 (p. 169).

Zhou, G., & Kresta, S. M. (1996). Impact of tank geometry on the maximum turbulence energy dissipation rate for impellers. *American Institute of Chemical Engineering Journal*, *42*, 2476.